RMetS
Royal Meteorological Society

Ocean Rossby waves as a triggering mechanism for primary Madden–Julian events

Benjamin G. M. Webber[a]*, Adrian J. Matthews[a,b], Karen J. Heywood[a] and David P. Stevens[b]
[a]*School of Environmental Sciences, University of East Anglia, Norwich, UK*
[b]*School of Mathematics, University of East Anglia, Norwich, UK*

*Correspondence to: B. G. M. Webber, School of Environmental Sciences, University of East Anglia, Norwich NR4 7TJ, UK. E-mail: b.webber@uea.ac.uk

The Madden–Julian Oscillation (MJO) is sporadic, with episodes of cyclical activity interspersed with inactive periods. However, it remains unclear what may trigger a Madden–Julian (MJ) event which is not immediately preceded by any MJO activity: a 'primary' MJ event. A combination of case-studies and composite analysis is used to examine the extent to which the triggering of primary MJ events might occur in response to ocean dynamics. The case-studies show that such events can be triggered by the arrival of a downwelling oceanic equatorial Rossby wave, which is shown to be associated with a deepening of the mixed layer and positive sea-surface temperature (SST) anomalies of the order of 0.5–1 °C. These SST anomalies are not attributable to forcing by surface fluxes which are weak for the case-studies analysed. Furthermore, composite analysis suggests that such forcing is consistently important for triggering primary events. The relationship is much weaker for successive events, due to the many other triggering mechanisms which operate during periods of cyclical MJO activity. This oceanic feedback mechanism is a viable explanation for the sporadic and broadband nature of the MJO. Additionally, it provides hope for forecasting MJ events during periods of inactivity, when MJO forecasts generally exhibit low skill.

Key Words: equatorial Rossby waves; Indian Ocean dynamics; intraseasonal variability

Received 28 February 2011; Revised 14 June 2011; Accepted 26 August 2011; Published online in Wiley Online Library 4 October 2011

Citation: Webber BGM, Matthews AJ, Heywood KJ, Stevens DP. 2012. Ocean Rossby waves as a triggering mechanism for primary Madden–Julian events. *Q. J. R. Meteorol. Soc.* **138**: 514–527. DOI:10.1002/qj.936

1. Introduction

Equatorial Rossby and Kelvin waves form a large part of tropical ocean variability at time-scales ranging from intraseasonal (Kessler *et al.*, 1995; Hendon *et al.*, 1998) to interannual (Battisti, 1988; McPhaden, 1999). Such waves affect sea surface height (SSH), zonal currents, pycnocline depth and vertical velocities. Anomalies in mixed-layer depth, along with vertical, meridional and zonal advection, lead to variability in heat content and sea surface temperatures (SSTs; McCreary, 1983; Battisti, 1988). These effects on SSTs allow the ocean dynamics to trigger atmospheric convection, leading to feedbacks which have been shown to be important for the El Niño–Southern Oscillation (ENSO; Battisti, 1988; Kessler and McPhaden, 1995; McPhaden, 1999) as well as for the Madden–Julian Oscillation (MJO; Han *et al.*, 2001; Webber *et al.*, 2010).

Baroclinic waves perturb the depth of the mixed layer by several orders of magnitude more than they affect SSH. Thus, although typical SSH anomalies associated with equatorial Kelvin and Rossby waves are of order 10 cm (Giese and Harrison, 1990), thermocline depth can vary by as much as 40 m (Kessler *et al.*, 1995; McPhaden, 1999). This depth anomaly is of the opposite sign to the SSH perturbation, such that waves with a positive SSH signal correspond to a deeper mixed layer. It is common to describe baroclinic waves associated with positive SSH anomalies and a deeper mixed layer as 'downwelling' waves.

We adopt this terminology here, although it should be noted that such a wave is associated with both downwelling (at the leading edge) and upwelling (at the trailing edge) anomalies. Similarly, baroclinic waves with negative SSH anomalies and a shallower mixed-layer depth are termed 'upwelling' waves.

Equatorial waves are forced by anomalies in surface wind stress. A symmetric westerly wind burst along the Equator will generate Ekman convergence at the Equator and thus force downwelling anomalies which then propagate eastward as a Kelvin wave (Battisti, 1988; Giese and Harrison, 1990). Typically, such wind bursts will also force a westward-propagating Rossby wave of the opposite sign, although this is dependent on the meridional structure of the wind field and its resultant curl (Chelton *et al.*, 2003). The meridional component of the wind field can also affect the magnitude of the resultant Rossby waves.

The MJO is the dominant mode of tropical atmospheric variability at intraseasonal time-scales, and is thus an important source for intraseasonal oceanic Rossby and Kelvin wave activity. The MJO is characterised by propagating atmospheric wave structures affecting convection, surface and upper-tropospheric winds, surface fluxes and influencing rainfall throughout the Tropics and worldwide (Madden and Julian, 1971, 1972; Matthews *et al.*, 2004; Donald *et al.*, 2006). The MJO has a broadband spectral signal, with the most energy in the 40–60 day range (Madden and Julian, 1971, 1972), but with a low-frequency tail extending as far as 100 days (Salby and Hendon, 1994). Zhang (2005) and Lau and Waliser (2005) provide full reviews of the MJO.

The MJO has a substantial effect on SSTs through variations in surface fluxes, which has led to the suggestion that coupled ocean–atmosphere processes could be an important component of the MJO. The relative importance of ocean feedbacks as opposed to atmospheric-only mechanisms remains contentious (Zhang, 2005). However, models incorporating atmosphere–ocean coupling tend to outperform atmosphere-only models, although the degree of improvement varies from minimal (Hendon, 2000) to substantial (Inness and Slingo, 2003). Realistic MJO behaviour arises in atmosphere-only models forced by intraseasonal SST anomalies (Woolnough *et al.*, 2001; Fu and Wang, 2004; Matthews, 2004), reinforcing the notion that there is at least the potential for SST anomalies to exert a strong influence on MJO activity. The standard hypothesis for this thermodynamic feedback is that the SST anomalies are in quadrature with the convective anomalies (Shinoda *et al.*, 1998) such that the positive SST anomalies exist to the east of the enhanced convection and negative SST anomalies exist to the east of the reduced convection, thus leading to eastward propagation (Flatau *et al.*, 1997; Woolnough *et al.*, 2000). The magnitude of these flux-induced intraseasonal SST anomalies is ∼0.15–0.35 °C in composites of the MJO (Shinoda *et al.*, 1998). In the Indian Ocean, this ocean–atmosphere interaction is strongest for the low-frequency component of the MJO which is strongest during boreal winter when the convection shifts southward over the Seychelles–Chagos thermocline ridge (Izumo *et al.*, 2010).

In addition to this thermodynamic coupling mechanism, there is also the potential for the ocean dynamics to force the MJO (Han *et al.*, 2001; Fu, 2007; Webber *et al.*, 2010). In the Indian Ocean, the dynamical ocean response to the MJO consists of equatorial Kelvin waves which reflect into equatorial Rossby waves on reaching the coast of Sumatra (Oliver and Thompson, 2010; Webber *et al.*, 2010). These reflected Rossby waves propagate westwards to arrive in the western Indian Ocean approximately 90 days later, where they lead to positive SST anomalies and thus trigger convection within the region where MJO events are initiated (Webber *et al.*, 2010). The magnitude of these composite warm anomalies is similar to the flux-induced anomalies, being around 0.2 °C in the absence of strong surface heat fluxes. This dynamical ocean forcing mechanism is one of many triggers for MJO events, but is expected to modulate MJO activity and enhance the low-frequency component of the MJO.

This article seeks to examine whether forcing from ocean Rossby waves can also explain another feature of the MJO, namely the existence of 'primary' Madden–Julian (MJ) events (Matthews, 2008). One of the reasons for the broad spectral signal of the MJO is that it is sporadic, with periods of continuous MJO activity punctuated by periods with minimal or incoherent variability. Matthews (2008) defined primary MJ events as having no preceding cycle of the MJO; they may or may not then trigger one or many 'successive' MJ events. The key question is then to identify what causes primary events, but no conclusive triggering mechanism has been identified to date. In addition, forecasting the initiation of the MJO after periods of inactivity is notoriously difficult (Jones *et al.*, 2000), possibly due to the lack of understanding of the triggering mechanisms for primary events. However, the feedback from equatorial oceanic Rossby waves has not yet been examined in this light, which we will now address. Section 2 describes the datasets used in this study and section 3 defines the methodologies used. The results are outlined in section 4, starting with the results from primary case-studies, and then proceeding to composite studies of both primary and successive events. The conclusions are discussed in section 5.

2. Data

The SSH data used in this study are from the merged TOPEX/Poseidon–Earth Remote Sensing (T/P-ERS) satellite altimetry product (Fu *et al.*, 1994; Ducet *et al.*, 2000; Le Traon *et al.*, 2001). Weekly maps on a 0.25° grid were obtained for the period from 14 October 1992 to 23 January 2008, and then interpolated to daily values using cubic splines. This was done to facilitate comparison with other, daily, datasets. Geostrophic velocities were obtained from the same dataset and over the same period. SST data from the Tropical Microwave Imaging (TMI) satellite were extracted from 1 January 1998 to 17 December 2008. The data are available as daily maps of the 3-day average SST at 0.25° resolution. We have chosen the TMI dataset over other SST data since the data are not obstructed by clouds and thus are more accurate and contain more variance than SST datasets based on infrared measurements (Harrison and Vecchi, 2001; Klingaman *et al.*, 2008). Comparison with the Reynolds SST dataset (Reynolds *et al.*, 2007) suggests that the main conclusions of this work are not dependent on the choice of dataset.

In order to analyse sub-surface ocean variability associated with Rossby waves, we use an ocean state estimate derived from the ECCO-GODAE project (Estimating the Circulation and Climate of the Ocean–Global Ocean Data Assimilation Experiment; Wunsch and Heimbach, 2007). This is based on the Massachusetts Institute of Technology

(MIT) general circulation model (Marshall *et al.*, 1997a,b) and its adjoint (Heimbach *et al.*, 2005). It assimilates all available observations to provide the best estimate of ocean state while retaining dynamical consistency both internally and with atmospheric forcing (Wunsch and Heimbach, 2007). The model covers the world ocean between 80°N and 80°S, excluding the Arctic, at 1° horizontal resolution with 23 vertical levels. The ECCO data used in this study are the vertical velocities and density anomalies, along with SST data for comparison with the TMI dataset, all obtained at daily resolution for the period from 2 January 1992 to 30 December 2007.

Outgoing long-wave radiation (OLR) is used as a proxy for tropical deep convective precipitation. The OLR data for this study were obtained as 2.5° resolution gridded daily maps from the optimally interpolated Liebmann and Smith (1996) dataset from 1 January 1990 to 31 October 2008. For comparison with the OLR data, precipitation from the Tropical Rainfall Measuring Mission (TRMM) dataset was obtained for the period from 1 January 1998 to 31 May 2010. The main results of this paper are not sensitive to whether OLR or TRMM data are used; the OLR dataset is preferred for this study as it covers the entire period for which SSH data are available. Surface fluxes of latent and sensible heat, and short- and long-wave radiation were obtained from the European Centre for Medium-range Weather Forecasts (ECMWF) for the period of 1 January 1990 to 31 December 2008; net surface heat fluxes were then calculated from these separate components.

The linear trend, mean and first three harmonics of the annual cycle were removed point-wise from each dataset to produce detrended anomaly fields, which were then bandpass-filtered using a 20–200-day Lanczos filter. The use of such a broadband filter is motivated by its ability to exclude low-frequency climate signals as well as high-frequency noise, while retaining the MJO signal and the distinction between individual MJ events better than a narrower filter window (Matthews, 2000). The filter uses 241 symmetric weights, meaning that 120 days of data are lost at each end of the dataset. All datasets were further truncated so that an integral number of calendar years are retained, thus avoiding seasonal bias.

3. Methodology

Although it has become common to use the multivariate Wheeler–Hendon index (Wheeler and Hendon, 2004) to define the MJO, Matthews (2008) used a univariate definition of the MJO based solely on its convective signal. The motivation for this approach was to better isolate causes for the triggering of convection in primary MJ events and also to maximise the degree of independence in other atmospheric variables. We choose to use the same definition of the MJO and primary and successive MJ events as Matthews (2008), so that the results can be compared with that study. However, using the Wheeler–Hendon index produces broadly similar results.

The methodology of Matthews (2008) defines four phases of the MJO, with phase A representing the initiation of convection in the Indian Ocean coinciding with reduced convection in the western Pacific and phase B the propagation of enhanced convection over the Maritime Continent. Phases C and D are the inverse of phases A and B respectively. Periods of low MJO activity were classified as phase N, with a buffer zone to prevent a weak MJO from oscillating between active and inactive such that it is erroneously labelled a primary event (Matthews, 2008).

Table I. Start dates for primary and successive events for the period 1992–2009.

Year	Primary events	Successive events
1992	2 Dec	6 Feb, 28 Mar, 30 Apr
1993	30 Nov	15 Jan, 12 Feb, 28 May, 21 Jul
1994		15 Mar, 31 May, 29 Jun, 17 Nov
1995		8 Jan, 24 Feb, 27 Mar, 4 May, 6 Jun
1996		26 Mar, 26 Apr, 8 Jun, 5 Jul, 10 Oct, 7 Dec
1997	12 Feb	31 Mar, 10 May
1998	29 Oct	
1999	22 Aug	20 Jan, 17 Mar, 11 Oct, 2 Dec
2000	20 Feb	2 Aug, 18 Nov
2001	26 Apr	29 Jul
2002		1 May, 1 Aug, 1 Oct, 12 Nov, 22 Dec
2003	7 Dec	4 May, 2 Oct
2004	24 Sep	27 Dec
2005	30 Mar	29 Aug, 11 Oct
2006	21 Mar	10 Jan, 18 Apr, 9 Sep, 23 Dec
2007	29 Apr, 20 Jul	12 Dec
2008	26 Aug	18 Mar, 18 Apr
2009		27 Jan, 9 Apr, 9 Nov

Primary events are thus defined using the above terminology by the phase sequence NABCD, and successive events by DABCD. Whether either type of event is followed by another MJO event is not considered in this study, although understanding MJO events which are not followed by another ('terminal events') is a worthwhile avenue of future study. A list of the start dates of primary and successive events is provided in Table I. Note that the dates for each event correspond to the maximum principal component (PC) amplitude in phase A, which refers to convection within the Indian Ocean. Matthews (2008) showed that this is the most common region for primary MJ events to occur, but it is possible for primary events to be triggered elsewhere. It is therefore not necessary for a successive event to be preceded by a primary event as defined here; furthermore, it is also possible for successive events to follow a period of disjointed MJO activity that is neither 'successive' nor 'primary'.

Figure 1 shows composite Hovmöller diagrams of OLR anomalies over the warm pool of the western Pacific and the Indian Ocean for the dates defined in Table I. Although there are some positive OLR anomalies in the Indian Ocean prior to the initiation of primary events, these do not propagate or form part of a coherent MJ event. By contrast, for successive events, the preceding positive OLR anomalies propagate

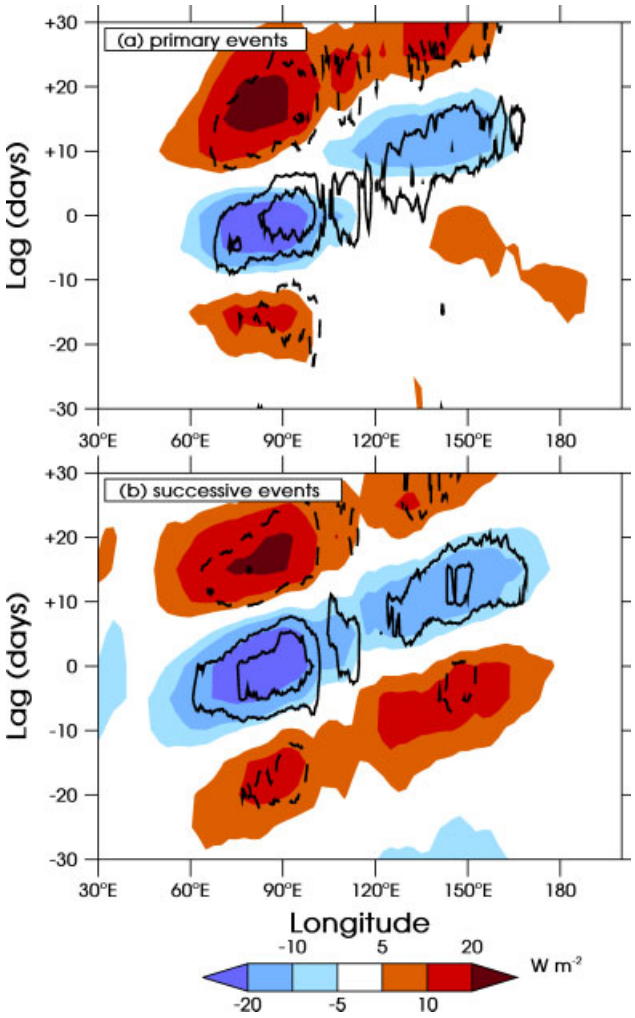

Figure 1. Hovmöller diagrams of anomalous OLR (shading; W m^{-2}) and TRMM precipitation (contours) from lagged composites for (a) primary and (b) successive MJ events. The TRMM contour interval is 0.1 mm h^{-1}, the zero contour is omitted and negative contours are dashed. This figure is available in colour online at wileyonlinelibrary.com/journal/qj

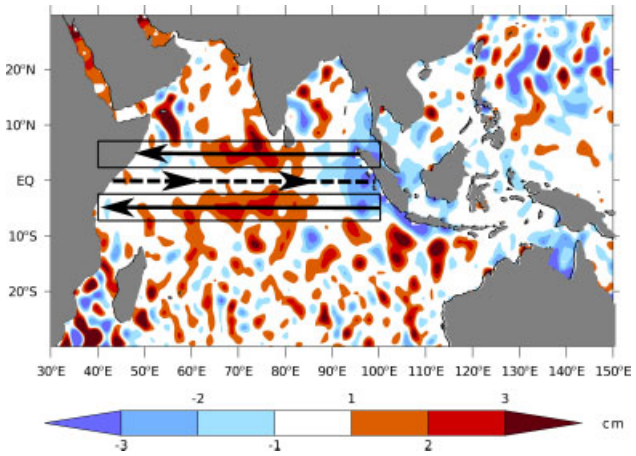

Figure 2. Composite SSH anomalies (cm) at lag −35 days relative to primary MJ events as defined in Table I, illustrating the propagation paths for equatorial Rossby waves (black boxes and solid arrows), and equatorial Kelvin waves (dashed arrow). The black boxes also represent the latitudes over which subsequent Hovmöller diagrams of Rossby wave propagation are calculated. This figure is available in colour online at wileyonlinelibrary.com/journal/qj

coherently across the entire warm pool. These results are consistent with those of Matthews (2008).

Figure 2 shows the propagation of Rossby and Kelvin waves in a composite of SSH at lag −35 relative to primary MJ events. The dashed arrow along the Equator shows the equatorial Kelvin waveguide, the black boxes and arrows the equatorial Rossby waveguide. These boxes are defined on the basis of the Rossby radius of deformation; first meridional mode Rossby waves typically have SSH maxima centred around 4° latitude away from the Equator (Chelton *et al.*, 2003). The positive SSH anomalies in the central Indian Ocean are associated with a downwelling Rossby wave, while the negative SSH anomalies near the Maritime Continent indicate the reflection of an upwelling equatorial Kelvin wave into an upwelling equatorial Rossby wave. The triggering of upwelling coastal Kelvin waves can also be seen at the eastern boundary. For the subsequent analysis of the effects of Rossby wave propagation, Hovmöller diagrams for the Rossby waveguide are constructed over the latitudes and longitudes indicated by the black boxes in Figure 2. Data over land are masked and therefore not included in the results.

For the case-study analysis, two representative primary events are selected, starting on 12 February 1997 and 24 September 2004. Relevant atmospheric and oceanic variables are extracted for the period extending from 100 days prior to the start date of these primary events to 100 days after. This allows the propagation of any Rossby waves to be followed across the Indian Ocean. The same time window is used for the compositing method, such that the composites represent the average of each variable over all the primary event case-studies. Composites are also produced for the successive events.

4. Results

4.1. *Case-studies*

Figure 3 shows two case-studies of primary MJ events. Figure 3(a, b, c) relate to the event starting 24 September 2004, and Figure 3(d, e, f) are for the event starting 12 February 1997. In both events, a downwelling equatorial Rossby wave (positive SSH anomalies) propagates westward between −100 and 0 days; this is indicated by the solid diagonal line in Figure 3(a,d), which is calculated using the methodology described in the appendix. This is then followed by the initiation of the MJO convection, around 0 days, shown by the eastward-propagating negative OLR anomaly in the same panels. Note that although the OLR anomaly appears to be zonally uniform due to the aspect ratio, it is in fact propagating east at around 5 m s^{-1}, consistent with previous observations of the MJO (Zhang, 2005).

A key result of this article is that, in both of these case-studies, the initiation of the primary MJ events coincides with the arrival of the downwelling Rossby waves in both space and time. This is consistent with the mechanism proposed by Webber *et al.* (2010). However, it is likely that such oceanic forcing will be most important, and most apparent in observations, when other triggering mechanisms are weak or non-existent, such as is the case for primary events (Matthews, 2008).

In order for the ocean dynamics to trigger an MJ event, the downwelling waves must create positive SST anomalies of relatively large magnitude, i.e. of similar magnitude to

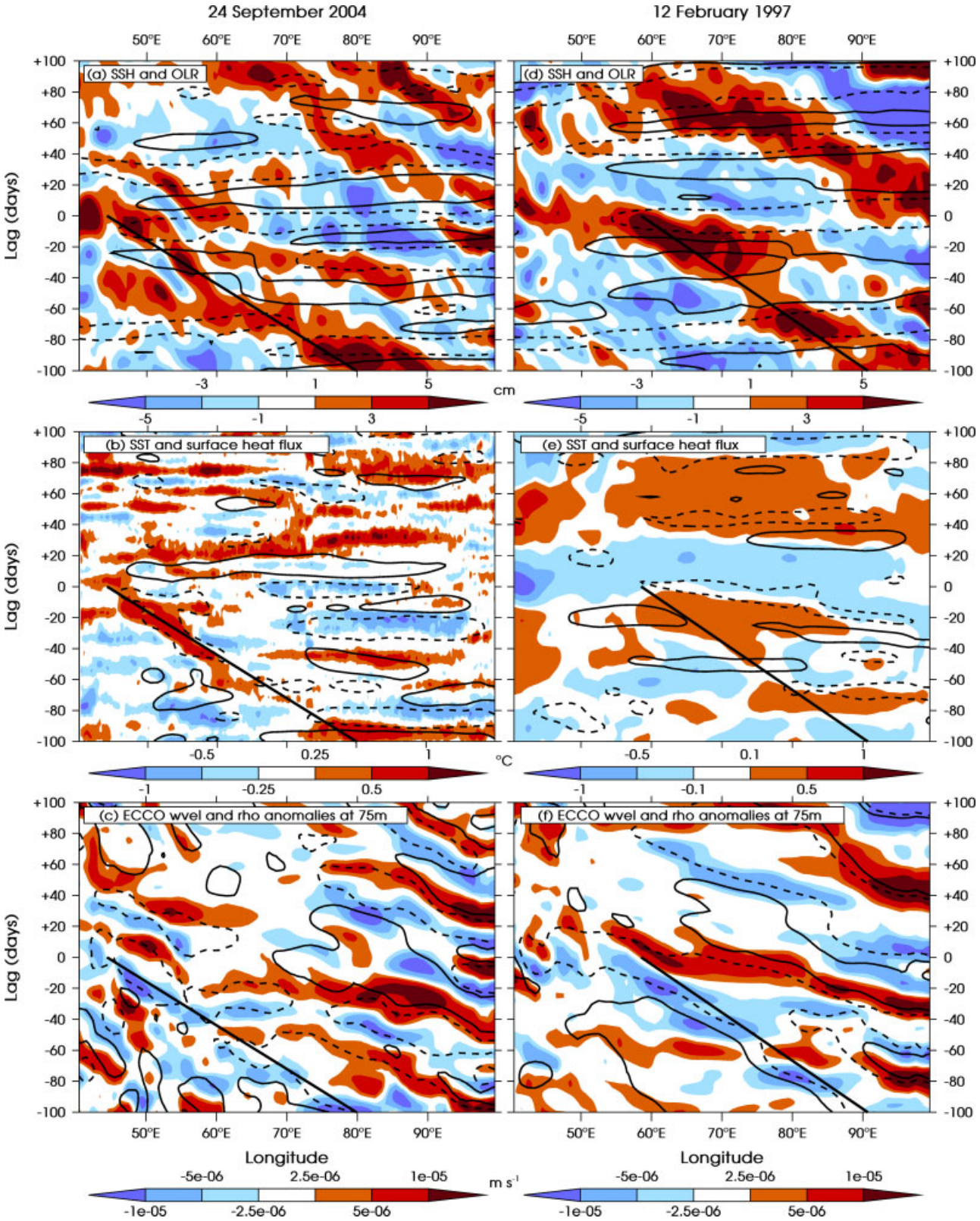

Figure 3. Hovmöller diagrams at lags −100 to +100 days relative to the primary event starting on 24 September 2004 of anomalous (a) SSH (shading, cm) and OLR (contours with interval 15 W m^{-2}), (b) SST (shading, °C) and surface flux (contours with interval 30 W m^{-2}), (c) ECCO vertical velocity (shading, m s^{-1}) and density (contours with interval 0.1 kg m^{-3}). (d) to (f): as (a) to (c), but for the primary event starting on 12 February 1997. Negative contours are dashed and the zero contour is omitted. The anomalies are averaged over 2–6°S and 2–6°N, the equatorial Rossby wave boxes shown in Figure 2. The solid diagonal line in each panel represents the propagation of the downwelling Rossby wave (positive SSH anomalies) in (a) and (d). This figure is available in colour online at wileyonlinelibrary.com/journal/qj

those observed in response to surface fluxes. To study this, we use a combination of TMI SST where available (for the 24 September 2004 case-study) and ECCO SST elsewhere (for the 12 February 1997 case-study), along with vertical velocity and density data from ECCO. In both case-studies the positive SSH anomalies are led by downwelling anomalies and coincide with negative density anomalies at 75 m (Figure 3(c,f)), consistent with a deepening of the mixed layer. This will increase the heat content of the mixed layer and lead to a reduction in the entrainment of cold subsurface waters through wind mixing (McCreary, 1983; Battisti, 1988). These effects lead to an increase in SST, as observed in the positive SST anomalies along the Rossby wave propagation path (Figure 3(b,e)).

Given that the initial triggering of convection for MJ events tends to be in the western Indian Ocean (e.g. Zhang, 2005), it is the region to the west of 75°E that is primarily of interest for oceanic triggering of primary events. In the classical model of thermodynamical air–sea interaction within the MJO (Flatau *et al.*, 1997; Shinoda *et al.*, 1998), SST anomalies would be expected to be in quadrature with the heat flux anomalies. There is some evidence of this in the eastern Indian Ocean (east of 70°E in Figure 3(b,e)), where there are zonally extensive flux anomalies that generally precede SST anomalies of the same sign. However, there are some SST anomalies that are not well explained by the surface fluxes, especially in the western Indian Ocean. For the case-study of 24 September 2004, the SST anomalies between lag −50 and lag 0, 40–60°E (Figure 3(b)) are consistent with the location and propagation of the downwelling anomalies (Figure 3(c)). In addition, these SSTs are not consistent with the surface flux anomalies, which are negative and appear to arise *in response* to the higher SSTs. The magnitude of the SST anomalies within this region of interest is around 0.5–1 °C, which is substantial for intraseasonal SST anomalies, and certainly sufficient to generate MJO-like convection (Woolnough *et al.*, 2001; Fu and Wang, 2004; Matthews, 2004). In addition, the coherent propagation of these SST anomalies from lead times as long as 50 days is impressive compared with other mechanisms for the MJO, with potential implications for forecasting such events.

Direct SST observations from the TMI dataset were not available for the case-study of 12 February 1997, so SST data from the ECCO reanalysis were used. These were compared with TMI SST data for other case-studies and found to be consistent, although the magnitude of the ECCO anomalies was consistently about 50% smaller than the observed TMI anomalies. In addition, due to the lower resolution of the ECCO data, these SST anomalies have less small-scale noise than those derived from TMI data. For the case-study starting 12 February 1997, the positive SST anomalies are preceded by some positive heat fluxes (Figure 3(e)). However, the shape and extent of the positive SST anomalies agree better with the density and vertical velocity anomalies in Figure 3(f) than with the surface fluxes, consistent with predominantly dynamic, as opposed to thermodynamic, forcing. The magnitude of these SST anomalies is between 0.2 and 0.5 °C; given that these are likely to be an underestimate of the true anomalies, they are certainly large enough to influence atmospheric convection.

Rossby waves have a variety of meridional modes; the first such mode is associated with symmetric off-equatorial maxima (Chelton *et al.*, 2003) and appears to dominate the intraseasonal ocean dynamics over the higher modes which have more complicated structures (Webber *et al.*, 2010). The distance by which the SSH maxima of the first meridional mode Rossby waves are displaced from the Equator is governed by the Rossby radius of deformation, but typically is of the order of 4–5° latitude (Chelton *et al.*, 2003). Analysis of the latitudinal structure of the Rossby waves observed here is consistent with first meridional mode waves.

The phase speed c of Rossby waves is governed by the baroclinic and meridional mode of the wave and by the stratification of the background state ocean through which it propagates. Equatorial Rossby waves (first baroclinic mode) follow the dispersion relation

$$c = \frac{-\beta}{k^2 + (2n+1)\beta/c_e}, \tag{1}$$

where $\beta \approx 2.3 \times 10^{-11}\,\mathrm{m^{-1}s^{-1}}$ is the meridional gradient of planetary vorticity, k is the zonal wavenumber, n is the meridional mode number and c_e is the phase speed of the first baroclinic mode Kelvin wave. Kelvin waves are non-dispersive; typical values of c_e are around 2.4–3.0 m s^{-1}, depending on local stratification (Chelton *et al.*, 1998). Long Rossby waves with small k are approximately non-dispersive, with $n = 1$ Rossby waves propagating at 1/3 of the Kelvin wave phase speed, or approximately 0.9 m s^{-1}. However, in reality, the Rossby wave phase speed is often weakly dependent on k such that for wavelengths of the order of 3000 km, c will be ∼15% lower than in the non-dispersive limit. Furthermore, Chelton *et al.* (2003) observed low-frequency, first meridional mode Rossby waves to propagate roughly 30% slower than predicted in the Pacific, giving phase speeds of around 0.5–0.6 m s^{-1}, even though these waves were approximately non-dispersive.

The phase speed of the Rossby waves we observe can be estimated from the slope of the lines in Figures 3(a,d). For both case-studies, the wave travels approximately 35° longitude in 100 days, leading to a phase speed of 0.5 m s^{-1}. We estimate the uncertainty in this estimate to be roughly ±0.1 m s^{-1}. This is slower than the non-dispersive first meridional, first baroclinic mode Rossby wave speed of around 0.9 m s^{-1} for this region (Chelton *et al.*, 1998). However, given that the wavelength of these waves is approximately 15–30° longitude, dispersive modifications to the phase speed will be non-negligible. Using a wavelength of 20° longitude, Eq. (1) gives a phase speed of 0.7 m s^{-1} for $c_e = 2.7$ m s^{-1}, which is not inconsistent with the phase speed observed. Zonal currents may influence the phase speed of these waves although, away from the Somali Current, the time-mean depth-averaged zonal velocity preceding the two case-studies is negligible. However, Chelton *et al.* (2003) showed that consideration of the shear generated by the asymmetric equatorial current system of the Pacific slowed the propagation of Rossby waves by around 0.2 m s^{-1}, which may partly explain the discrepancy seen here.

The SSH anomalies are symmetric about the Equator (not shown), consistent with first meridional mode waves but, to confirm the baroclinic mode of the waves, it is necessary to examine their vertical structure. To analyse this, we show depth–longitude sections of density and vertical velocity, averaged over 2–6°S and 2–6°N (boxes in Figure 2), at lags −50 days to 0 (Figure 4). These show the propagation of a downwelling Rossby wave indicated by the westward propagation of negative density anomalies,

and highlighted by the black diagonal arrow. The inverse relationship between the density and SSH anomalies can also be seen, consistent with baroclinic wave theory. As the sign of the vertical velocity anomalies is uniform with depth, and the density anomalies are unimodal with a single maximum around the depth of the pycnocline (roughly 100 m), these waves are most likely first baroclinic mode waves.

The vertical velocity anomalies are broadly in quadrature with the density and SSH anomalies, such that downwelling (negative vertical velocity anomalies) occurs at the leading (western) edge of the westward-propagating negative density anomalies. Given that the ocean is stably stratified, with background mean density increasing with depth, this suggests that the density anomalies arise predominantly through vertical displacements of isopycnals, as opposed to lateral advection or surface buoyancy fluxes. Furthermore, estimating the temperature advection from ECCO data (not shown) suggests that vertical temperature advection dominates, although horizontal advection is of the same sign and contributes around 25% of the total advection in the top 100 m. The total mean temperature advection over this depth range corresponds to warming rates of up to 0.1 °C per day. Assuming that this layer is fairly well mixed, and seeing that these anomalies persist for more than 10 days, the total cumulative temperature advection is sufficient to cause the observed SST anomalies. In addition, the deepening of the mixed layer associated with this downwelling will inhibit the entrainment of cold, deep water, thus enhancing the positive SST anomalies (McCreary, 1983). From seasonally averaged density profiles, the density anomalies can be converted to estimated perturbations to isopycnal depth; the anomalies of $\sim 0.1\,\mathrm{kg\,m^{-3}}$ seen in Figure 4 correspond to vertical perturbations of ~ 5 m in the isopycnals at 75 m, consistent with vertical velocity anomalies equivalent to $\sim 1\,\mathrm{m\,day^{-1}}$ sustained over several days.

The anomalies in both vertical velocity and density extend down below 300 m (Figure 4(f)), associated with downward propagation of wave energy into the deep ocean, consistent with the results of Matthews *et al.* (2007, 2010). The westward tilt of the anomalies with depth is consistent with upward phase propagation and downward energy propagation. Because the vertical density gradients are less in the deep ocean, the magnitude of the density anomalies decreases with depth, but there are nevertheless anomalies of around $0.005\,\mathrm{kg\,m^{-3}}$ at 1000 m, which is similar to the amplitude of the seasonal cycle at this depth (not shown).

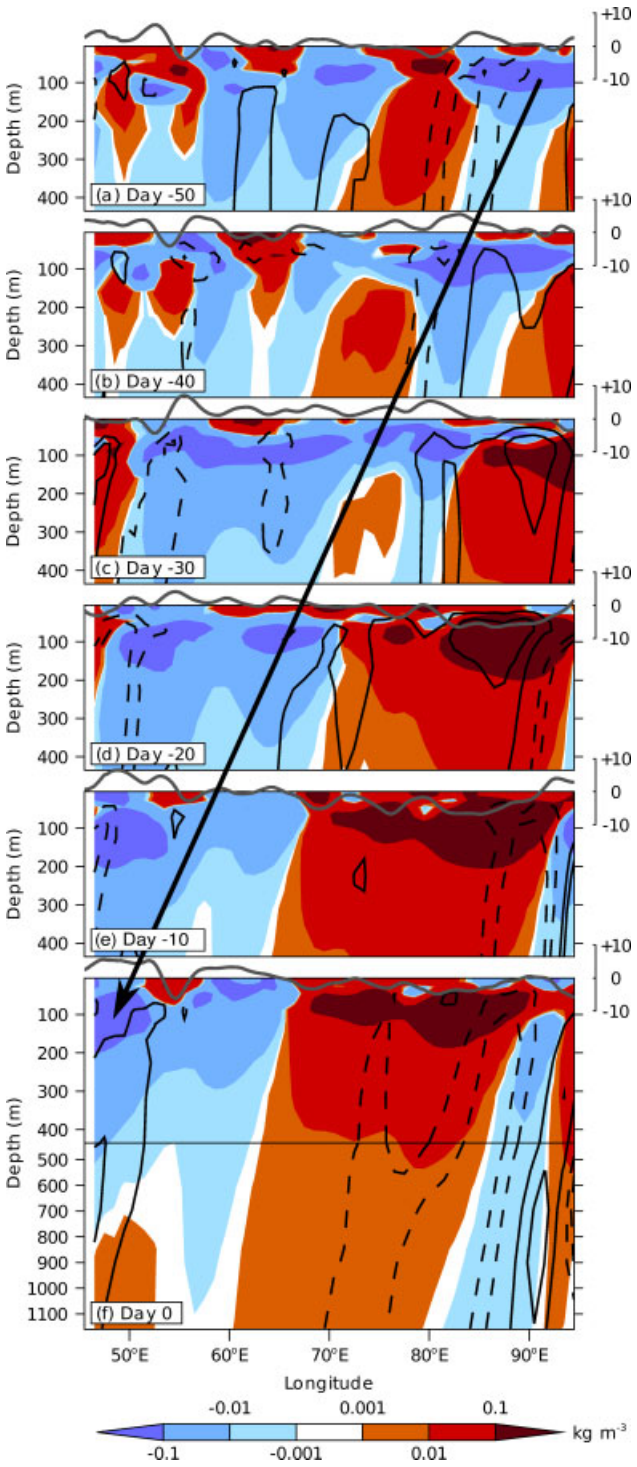

Figure 4. Density anomalies (shading, $\mathrm{kg\,m^{-3}}$), vertical velocity anomalies (black contours with interval $1 \times 10^{-5}\,\mathrm{m\,s^{-1}}$, negative contours dashed and the zero contour omitted) and SSH anomalies (grey contour along top of each panel, cm) at day (a) −50, (b) −40, (c) −30, (d) −20, (e) −10, and (f) 0 relative to the primary event on 24 September 2004. (f) is extended down to 1160 m to show the magnitude of the anomalies in the deep ocean; note the discontinuity in the *y*-axis at 435 m. The diagonal arrow indicates the propagation of the downwelling Rossby wave that triggers the primary event, and is calculated using the algorithm described in the Appendix. This figure is available in colour online at wileyonlinelibrary.com/journal/qj

4.2. *Composites*

The case-studies show the potential for primary MJ events to be triggered by the arrival of downwelling Rossby waves. Here, we examine how robust the relationship is in general through composite analysis. Figure 5 shows composites of the same variables as in Figure 3; Figure 5(a, b, c) are composites over all primary MJ events, and Figure 5(d, e, f) are for successive MJ events. For the SST data, the TMI data were available only for primary events after 1998, but this contains 14 out of the 17 events used for the other composites.

Figure 5(a) shows that primary MJ events, as indicated by the negative (dashed) OLR contour at around lag 0, are consistently preceded by the arrival of a downwelling Rossby wave (westward-propagating positive SSH anomaly), supporting the hypothesis of such waves as a triggering mechanism. The wave signal is relatively coherent, although a little discontinuous, and is preceded by downwelling anomalies and colocated with negative density perturbations at 75 m (Figure 5(c)), consistent with deepening of the mixed layer. The propagation speed of the composite wave

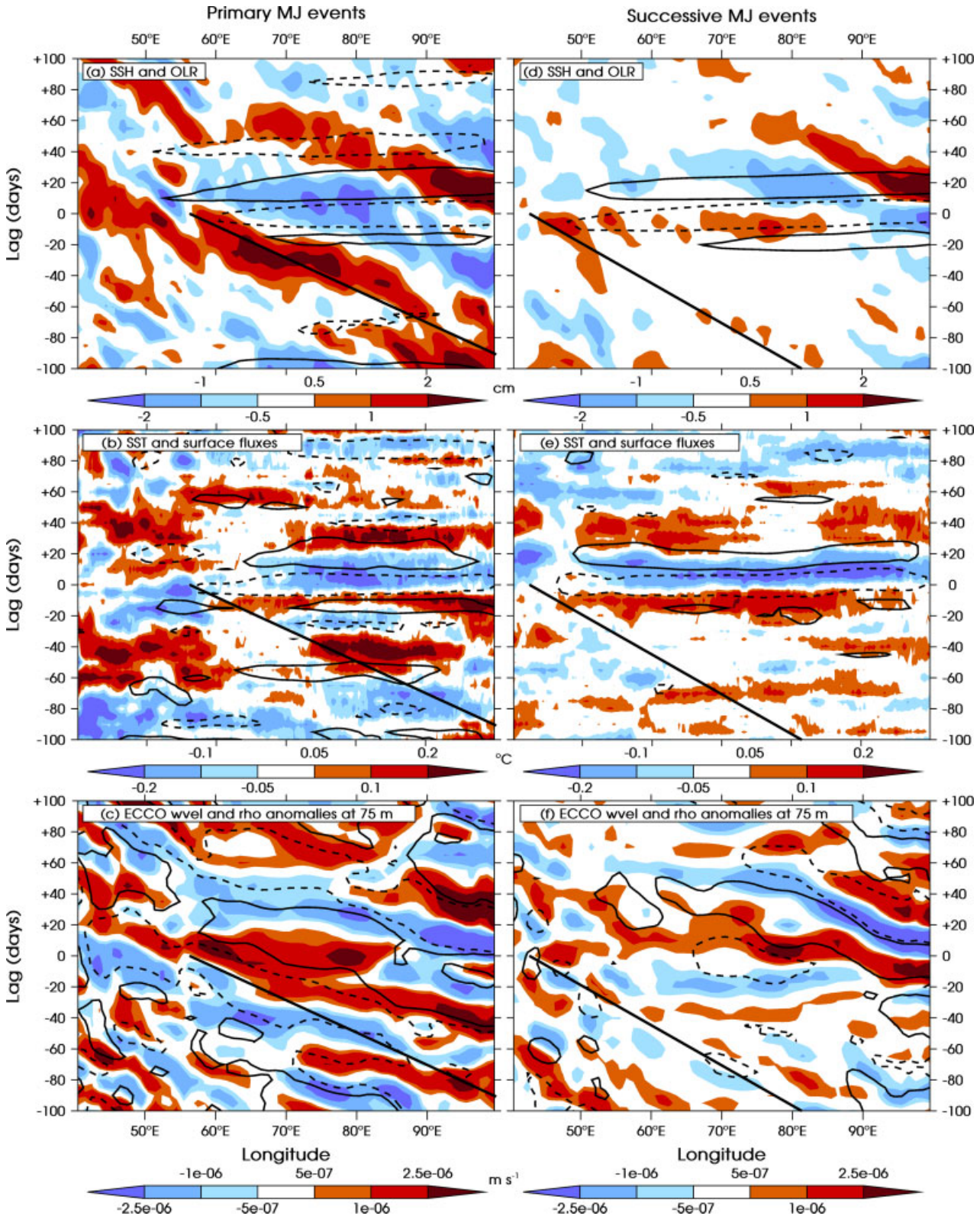

Figure 5. As Figure 3, but for (a, b, c) composite primary events and (d, e, f) composite successive events. The contour intervals are (a, d) $\pm 7.5\,\mathrm{W\,m^{-2}}$, (b, e) $\pm 10\,\mathrm{W\,m^{-2}}$, (c, f) $\pm 0.025\,\mathrm{kg\,m^{-3}}$. This figure is available in colour online at wileyonlinelibrary.com/journal/qj

is approximately $0.6\,\mathrm{m\,s^{-1}}$, slightly faster than in the case-studies. Both the OLR anomalies, and the positive SSH anomalies associated with the triggering Rossby wave, are statistically significant at the 95% confidence level.

The immediate relationship between SSH and SST anomalies is less clear for the composites than for the case-studies. There are positive SST anomalies in the region of interest (the western Indian Ocean) prior to the initiation of the primary MJ event, but they are relatively weak and do not propagate with the Rossby wave. Instead, the SST anomalies are zonally extensive and appear broadly consistent with surface fluxes, even if the dynamical forcing is also a factor. This is possibly an artefact of the methodology since the dynamically forced SST anomalies will be relatively

localised compared with the zonally extensive flux-driven SST anomalies. Given that our definition of primary MJ events assigns day zero to peak OLR amplitude anywhere within the Indian Ocean, this may refer to MJ events triggered at a wide range of longitudes. This could lead to dynamically induced SST anomalies being artificially 'smeared out' in the composite analysis; we return to this question below. Note that the propagating SSH signal of the Rossby wave is still evident despite this smearing effect because this signal is more coherent than for SST and also stronger relative to the zonally extensive wind stress forcing of SSH.

For successive MJ events, the composite analysis indicates a different story. There is little evidence of propagating Rossby wave signals, although the SSH anomalies are positive immediately prior to the initiation of the successive events (Figure 5(d)). The SST anomalies are zonally extensive (Figure 5(e)) and broadly consistent with the theories of thermodynamic air–sea interaction within the MJO (Flatau *et al.*, 1997; Shinoda *et al.*, 1998), and also consistent with the results of Matthews (2008), who found that successive MJ events were consistently preceded by significant positive SST anomalies. Note that both the primary and successive MJ events do themselves trigger Rossby waves at the eastern boundary of the Indian Ocean (positive SSH anomalies propagating westward from lag 10 days, 100°E), in keeping with the findings of Oliver and Thompson (2010) and Webber *et al.* (2010).

Figure 6 shows the depth–longitude sections of density and vertical velocity anomalies for the composite primary events. The vertical velocities are clearly in quadrature with the density anomalies, consistent with vertical motions being the primary cause of the density anomalies. These anomalies extend below 300 m, with composite density anomalies of up to 0.0025 kg m^{-3} at 1000 m; there is also a pronounced westward tilt with increasing depth below 500 m (Figure 6(f)), consistent with downward propagation of wave energy. Once again, the vertical structures of these waves support the hypothesis that they are first baroclinic mode waves whose phase speeds have been slowed by a combination of basic state currents and dispersive effects.

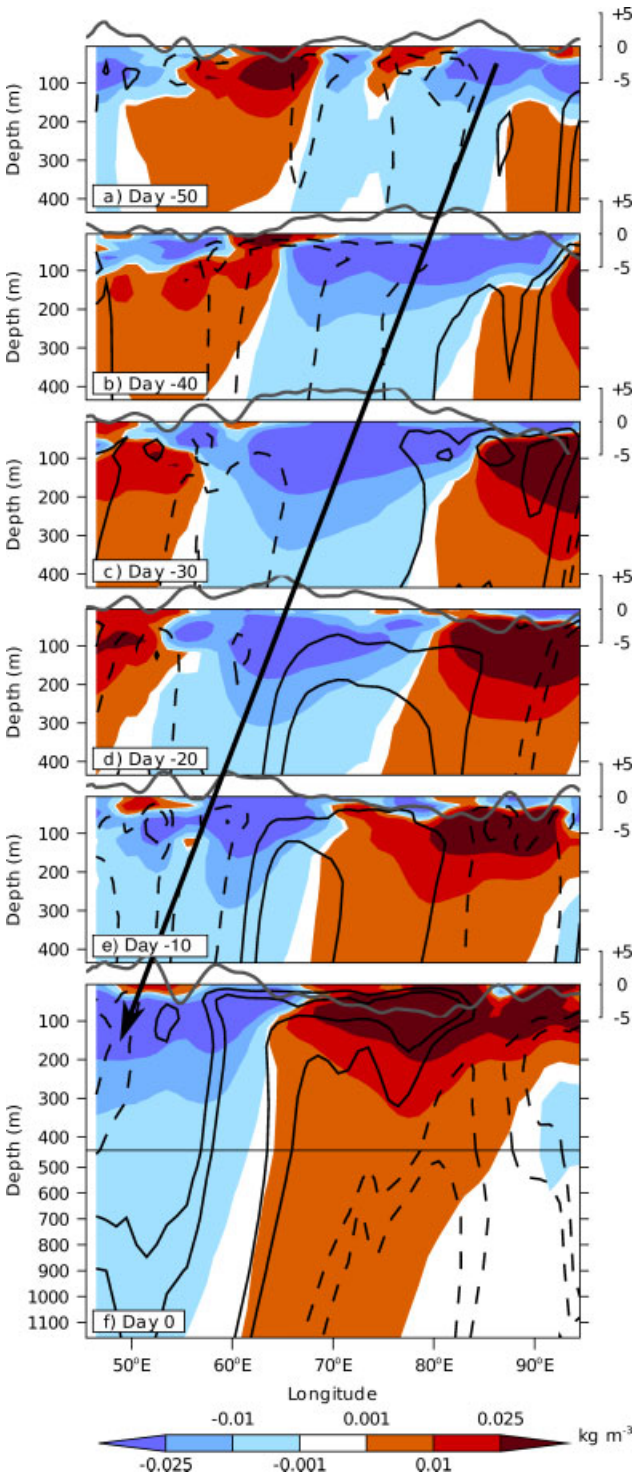

Figure 6. As Figure 4, but for composite primary events. The contour interval for the vertical velocity anomalies is 2.5×10^{-5} m s^{-1}. This figure is available in colour online at wileyonlinelibrary.com/journal/qj

4.3. *Relative longitude*

As discussed above, there is the potential for primary MJ events to be triggered at different longitudes; therefore the triggering Rossby wave signals will not be aligned in longitude, leading to a tendency for composite analysis to smear out the signal. This is especially true for variables such as SST anomalies where other, zonally extensive processes may mask the relatively localised influence of ocean dynamics. Indeed, analysis of the longitude of the arrival of the Rossby waves indicates a wide spread between 40 and 70°E, following a bimodal distribution with peaks around 45 and 65°E (not shown), although it is not clear why such a distribution would be produced. To account for this variability, the composites are aligned onto a new, relative longitude axis, such that the Rossby waves arrive at zero relative longitude. This methodology is described in the Appendix.

The results of the relative longitude composites are shown in Figure 7; the same variables are composited as in Figure 5. The composites extend only to relative longitude −5°, since any further extension to the west starts to impinge on Africa for many of the composite members. By construction, the SSH composite shows a westward-propagating positive SSH anomaly arriving on lag 0 days and zero relative longitude, for both primary (Figure 7(a)) and successive (Figure 7(d)) events. For primary MJ events, the propagating Rossby wave signal (positive SSH anomaly) is stronger and more coherent when expressed in relative longitude (Figure 7(a)) than in the 'true longitude' composite (Figure 5(a)). The phase speed of the composite Rossby wave is roughly 0.5 m s^{-1}, as in the case-studies. Note that the location of initiation

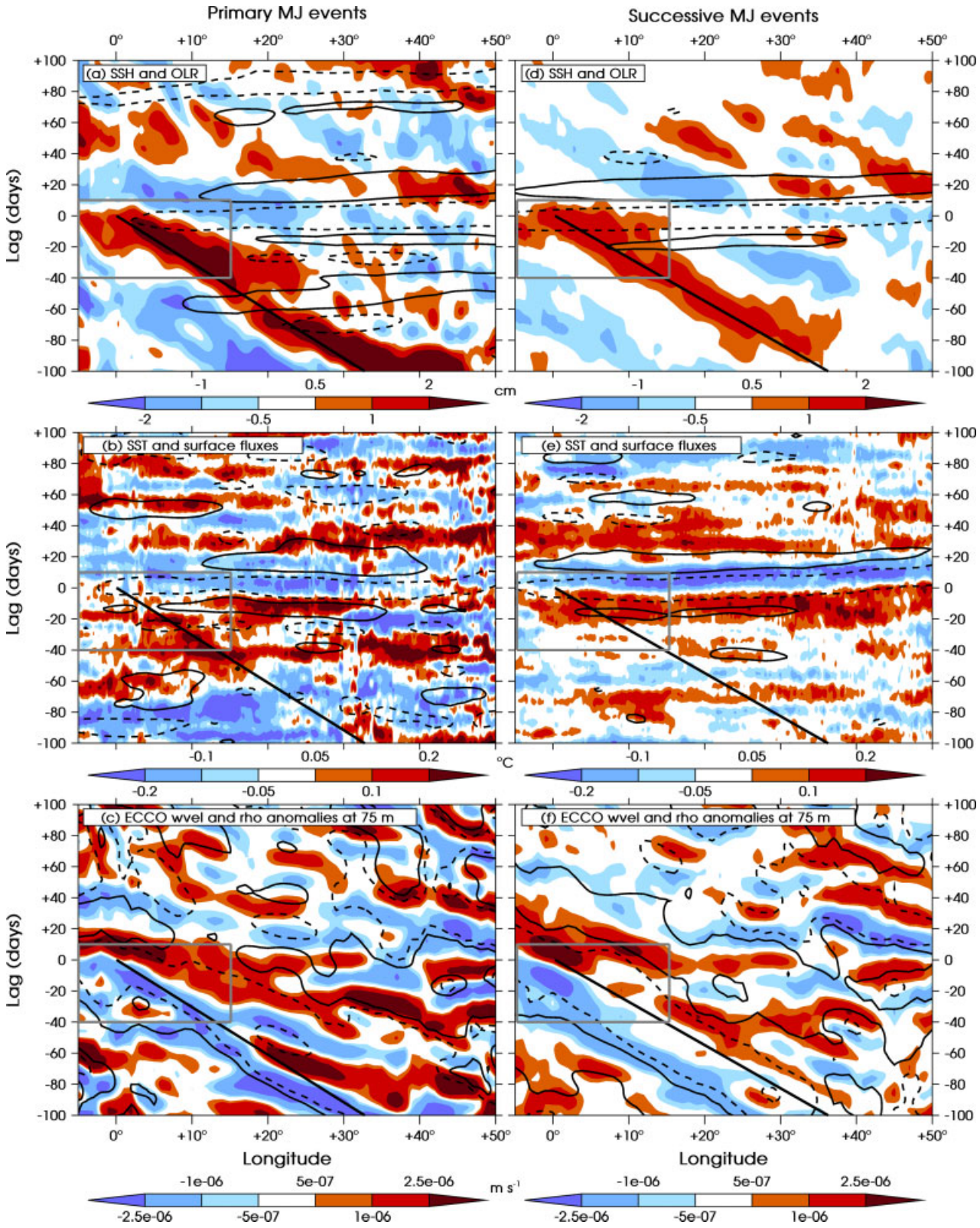

Figure 7. As Figure 5, but using relative longitude on the *x*-axis (Appendix A gives details). The grey box represents the area of particular interest in the western Indian Ocean where the downwelling Rossby wave has the greatest potential to trigger MJ events. This figure is available in colour online at wileyonlinelibrary.com/journal/qj

for the primary MJ event, as defined by the negative OLR anomalies, is not constrained in any way by this compositing methodology. Therefore, the fact that the OLR anomalies in Figure 7(a) do begin very close to relative longitude 0 reinforces the hypothesis that such events are triggered by the arrival of the Rossby wave.

Furthermore, once the downwelling Rossby wave arrives in the western Indian Ocean, where the thermocline is shallower, it is now colocated with coherently propagating SST anomalies (Figure 7(b), in the region indicated by the grey box). These SST anomalies have magnitudes around 0.15 °C, similar in magnitude to the composite flux-driven

SST anomalies known to be important for thermodynamic air–sea coupling (Shinoda *et al.*, 1998; Figure 7(e)). These positive SST anomalies are generally not consistent with the surface flux anomalies, but are consistent with the vertical velocity and density anomalies at 75 m (Figure 7(c)), implying a dynamical forcing. The anomalies propagate coherently from 50 days prior to the triggering of the primary event, suggesting potential predictability. There is still some evidence for flux-driven SST anomalies in the eastern Indian Ocean prior to the primary event, but it is clear that the dynamically driven SSTs play a crucial role in the initiation of the primary events.

When successive MJ events are composited on relative longitude, there is also a coherent Rossby wave signal (Figure 7(d)). This is perhaps not surprising, given that the methodology will locate any Rossby wave activity, whether or not such waves act as a trigger for convection. However, there is no coherent propagation of SST anomalies along the path of the Rossby wave signal; the SST anomalies are zonally homogeneous and consistent with surface flux forcing (Figure 7(e)). There are substantial vertical velocity and density anomalies at depth (Figure 7(f)), so it is somewhat surprising that a stronger SST signal is not seen. Consistent with this lack of a dynamically forced SST signal, the negative OLR anomalies begin substantially further west than the longitude of the Rossby wave signal at lag 0, out to –15° relative longitude (not shown). Hence, the arrival of the Rossby wave does not appear to be the primary trigger for successive MJ events. It is to be expected that the waves will still have an effect on the behaviour and frequency of successive events, but it is clear that other mechanisms are likely to be more important for successive events (Matthews, 2008).

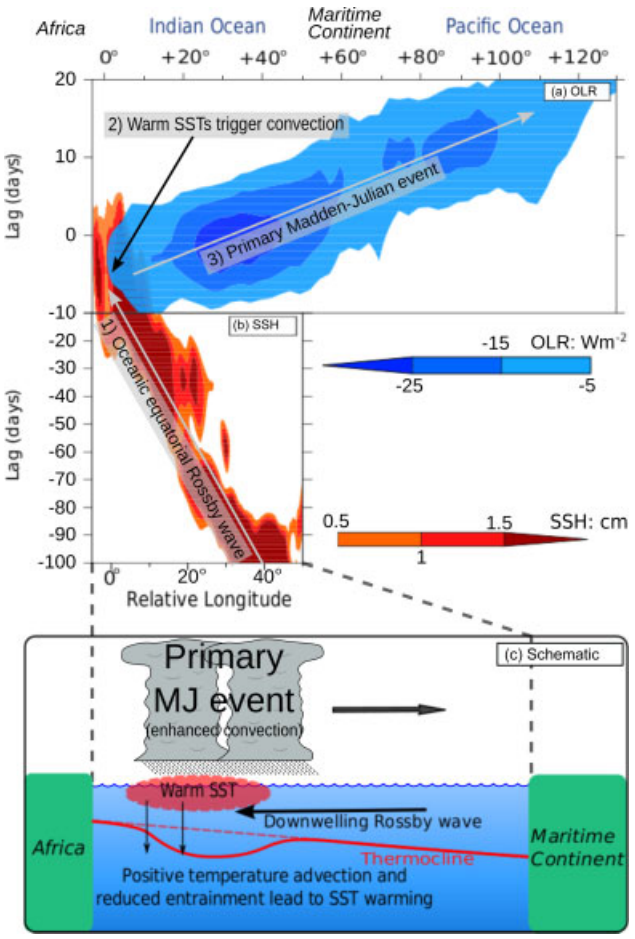

Figure 8. Triggering of primary Madden–Julian events by an oceanic equatorial Rossby wave. Hovmöller diagrams of anomalies of (a) OLR and (b) SSH (shading; see legends) on relative longitude at lags −100 to +20 days relative to composite primary MJ events. Note the discontinuity in the *y*-axis at lag −10 days. (c) Schematic of triggering mechanism for primary MJ events, showing the relationships between the Rossby wave (positive SSH anomalies in (a) and (b)), downwelling, thermocline depth and SSTs which leads to the triggering of a primary MJ event, as shown by the negative OLR anomalies in (a). This figure is available in colour online at wileyonlinelibrary.com/journal/qj

5. Conclusions

The key conclusion of this article is that primary MJ events can be triggered by the arrival of a downwelling ocean Rossby wave. This is supported by case-study and composite analysis. Given that no consistent trigger mechanism was found by Matthews (2008), this is substantial evidence for the importance of ocean dynamics for the MJO, as suggested by Webber *et al.* (2010). Such feedbacks are likely to modulate MJO activity more generally, although observational evidence will be less clear when other triggering mechanisms are also important.

In contrast to primary events, successive MJ events do not appear to be consistently triggered by the arrival of a downwelling Rossby wave. This presents a slightly different perspective to that given by Webber *et al.* (2010), who suggested that forcing from oceanic Rossby waves would affect all MJ events, thus providing a feedback mechanism that would enhance low-frequency MJO variability. The results presented here suggest that this oceanic forcing of the MJO is far stronger for primary events (a subset of the events used by Webber *et al.*, 2010) than for successive events. Nevertheless, this will have the effect of strengthening the low-frequency tail of the MJO since the frequency composition of primary events is, by definition, lower. It is interesting to note that air–sea interaction has been observed to occur more strongly within a lower-frequency component of the MJO in the Indian Ocean (Izumo *et al.*, 2010).

Figure 8 shows the proposed triggering mechanism for primary MJ events. The downwelling Rossby wave propagates in from the eastern Indian Ocean; these waves may have been triggered by reflection of equatorial Kelvin waves at the eastern boundary, or by direct forcing from equatorial wind stress curl. The wind stress which initially triggers these waves may be related to previous MJO activity, well separated from the subsequent primary MJ event by a period of quiescence, but other sources of intraseasonal wind variability are also likely to be important. The triggering Rossby wave is associated with positive (predominantly vertical) temperature advection, along with deepening of the mixed layer and thus reduction in the entrainment of cold water to the surface, leading to an increase in SST. This SST increase leads to moistening and warming of the atmospheric boundary layer over a large region, thus priming the atmosphere for convection and triggering a primary MJ event. Although the schematic shows the waves triggering a new event only upon reaching the western Indian Ocean, analysis of individual case-studies suggests that events can be triggered anywhere between 40° and 70°E, where the MJO is typically triggered and the thermocline is relatively shallow.

It is interesting to examine these results in the light of previous studies of intraseasonal ocean dynamics in the

Indian Ocean. It has been suggested that the propagation of Rossby and Kelvin waves will couple to the atmosphere, thereby enhancing atmospheric convection at time-scales of around 90 days (Han *et al.*, 2001; Han, 2005; Fu, 2007), consistent with the idea that such feedbacks will enhance the low-frequency tail of the MJO. Oliver and Thompson (2010) and Webber *et al.* (2010) documented how the cyclical MJO can force equatorial Kelvin wave variability which subsequently generates both reflected Rossby waves and coastal Kelvin waves upon reaching the coast of Sumatra. In their composites based on the cyclical MJO, these Rossby waves do not coherently propagate as far as the western Indian Ocean. However, this is likely to be due to the fact that compositing on the cyclical MJO imposes a time-scale that is shorter than the time taken for a Rossby wave to cross the Indian Ocean. Indeed, time-lag composites relative to a single MJO phase do show Rossby waves freely propagating as far as the western Indian Ocean (Figure 5 of Webber *et al.*, 2010). Therefore, these previous studies do not preclude the possibility that the Rossby waves observed to trigger primary MJ events could have been triggered by MJO activity some time beforehand, followed by a period of inactivity.

Forecasts of the MJO generally perform better when there is already an active MJ event in existence (Jones *et al.*, 2000). This is consistent with the observation by Matthews (2008) that successive events are associated with a multitude of triggering mechanisms that are relatively well understood, in contrast to primary events. The results presented here suggest that an accurate knowledge of the ocean state could offer predictability for primary events, especially as the propagation of oceanic Rossby waves is predictable at long lead times (potentially several months). Indeed, recent ensemble prediction of the MJO using a coupled model that was initialised with both atmospheric and oceanic analyses has shown significant improvement in skill for times when there is no initial MJO activity, i.e. primary events (Rashid *et al.*, 2011). It would be interesting to analyse whether the inclusion of SSH data in statistical forecasts of the MJO also improves skill scores. The potential for Rossby waves to trigger a primary event will likely depend upon atmospheric conditions also being suitable for the generation of an MJ event. Nevertheless, the results presented here suggest that monitoring Rossby waves in the Indian Ocean, through a combination of data from moorings, ARGO floats and satellite altimetry, is a worthwhile undertaking that might help predict primary MJ events.

Another consideration that will affect the strength of this proposed forcing mechanism is the degree to which SSTs depend upon mixed-layer depth. For example, McPhaden (1999) noted that the shoaling of the thermocline following the 1997–1998 El Niño event only led to a reduction of SSTs once the wind-induced mixing increased sufficiently to entrain the cold deep waters to the surface. Therefore, it should be expected that the effect of downwelling (or indeed upwelling) waves on SSTs will be dependent on the degree of wind-induced mixing and the depth of the basic-state thermocline. However, given that the thermocline is relatively shallow in the western Indian Ocean, it follows that wind mixing will be relatively efficient at modifying SSTs here. Indeed, the western Indian Ocean is known to be a region where SSH and SST are well correlated (Xie *et al.*, 2002), thus making it a prime region for coupling between ocean dynamics and convection.

A limitation of this study is the small sample size available for primary MJ events, which increases the potential for sampling error in the results. This is unavoidable given the relatively short period over which satellite data have been available. Modelling studies of this dynamical forcing mechanism would be worthwhile, albeit contingent on the identification of a coupled model which adequately simulates all the relevant processes. Further work would also be useful to identify whether forcing by the ocean dynamics could also be responsible for 'terminal' events, where the MJO goes from active to inactive.

Acknowledgements

The altimeter products were produced by Ssalto/Duacs and distributed by Aviso with support from Centre national détudes spatiales (CNES) and are available at http://www.aviso.oceanobs.com/. The TMI SST data were obtained from the SSM/I website at http://www.ssmi.com/tmi/. The EMCWF surface flux data were obtained through the British Atmospheric Data Centre (BADC) and from the ECMWF website at http://data-portal.ecmwf.int/data/d/interim_daily/. The interpolated OLR data were obtained from the NOAA/OAR/ESRL PSD web site at http://www.cdc.noaa.gov/. TRMM rainfall data were obtained from http://trmm.gsfc.nasa.gov/. Data from the ECCO-GODAE project were obtained through the ftp://www.ecco-group.org/ site. BGMW was supported by a NERC PhD studentship. The research presented in this article was carried out on the High Performance Computing Cluster supported by the Research Computing Service at the University of East Anglia. We thank Matt Wheeler and an anonymous reviewer for comments that helped to improve the manuscript.

Appendix

We now describe the methodology used to create the relative-longitude composites. This methodology was designed to objectively identify the arrival of a downwelling Rossby wave at the start (i.e. lag 0) of each MJ event. For each MJ event, we identify the 'optimal' propagation line on the Hovmöller diagram of SSH anomalies over the Indian Ocean (40–100°E) between lag −100 days and lag 0 (e.g. Figure A.1(a) for MJ event starting on 12 February 1997). We assume that, for a Rossby wave to trigger a new MJ event, it must arrive in the *western* Indian Ocean, where the thermocline depth is shallower and large SST perturbations can be realised. Hence, only 'target' longitudes between 40 and 75°E are considered. We also assume that Rossby waves will have 'target' phase speeds only between –0.35 and –1.2 m s^{-1}, based on observations (Chelton *et al.*, 1998).

The best fitting target longitude λ, and phase speed c, is then determined for each case-study. A propagation line is constructed for each λ–c pairing, i.e. a line whose slope is determined by c, passing through longitude λ at lag 0. The SSH anomaly along this line is then calculated by interpolation from the data on the gridded Hovmöller diagram (Figure A.1(a)). The mean of this SSH section is then calculated. Once this process has been repeated for each possible pair of target longitudes and phase speeds, the mean SSH can be plotted on axes of target longitude and phase speed (Figure A.1(b)). The maximum value of mean SSH in this target longitude, phase speed parameter space is then

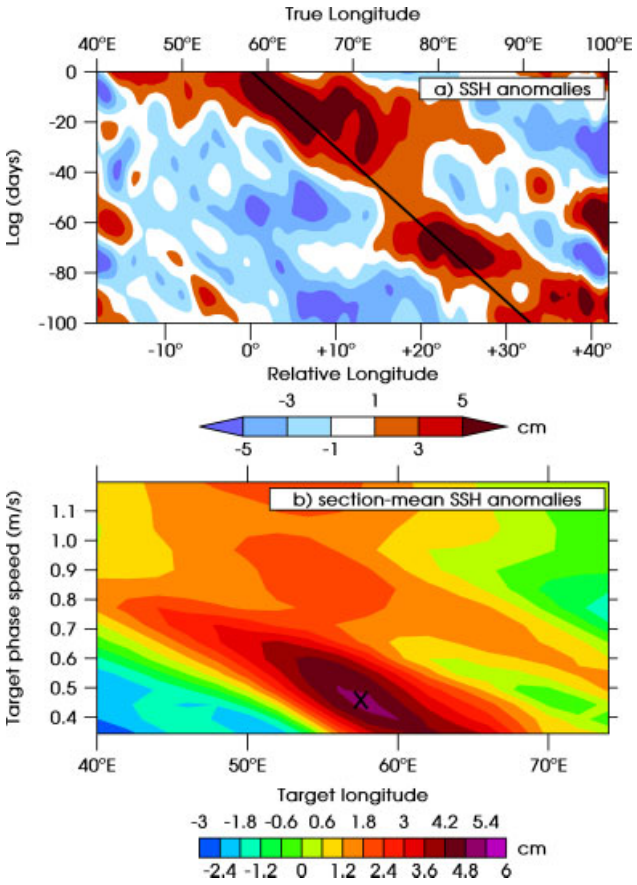

Figure A.1. Example of the methodology used to calculate relative longitude: (a) SSH anomalies (cm) for the primary event on 12 February 1997 with true longitude on the upper *x*-axis and the new, relative longitude on the lower *x*-axis. (b) Mean along-path SSH anomalies for the range of target longitudes and phase speeds used in the method. The maximum mean SSH is indicated by the solid line in (a) and the cross in (b). This figure is available in colour online at wileyonlinelibrary.com/journal/qj

found, and used to identify the optimal propagation line. For the example MJ event of 12 February 1997, this corresponds to a target longitude of 58°E, and a target phase speed of $-0.44\,\mathrm{m\,s^{-1}}$ (cross in Figure A.1(b)). When this optimal propagation line is plotted on the input Hovmöller diagram (diagonal line in Figure A.1(a)), it can be clearly seen to capture the westward-propagating positive SSH anomaly.

The methodology is robust in that the example shown here has a clear unimodal maximum that can be identified from the parameter space diagram (Figure A.1(b)). Results for other case-studies were similar.

The target longitude for each MJ event was then used to remap variables onto a relative longitude axis. Hence, the target longitude corresponds to a relative longitude of zero, and points to the west (east) of the target longitude correspond to negative (positive) relative longitudes.

References

Battisti DS. 1988. Dynamics and thermodynamics of a warming event in a coupled tropical atmosphere ocean model. *J. Atmos. Sci.* **45**: 2889–2919.

Chelton DB, DeSzoeke RA, Schlax MG, El Naggar K, Siwertz N. 1998. Geographical variability of the first baroclinic Rossby radius of deformation. *J. Phys. Oceanogr.* **28**: 433–460.

Chelton DB, Schlax MG, Lyman JM, Johnson GC. 2003. Equatorially trapped Rossby waves in the presence of meridionally sheared baroclinic flow in the Pacific Ocean. *Prog. Oceanog.* **56**: 323–380.

Donald A, Meinke H, Power B, Maia ADN, Wheeler MC, White N, Stone RC, Ribbe J. 2006. Near-global impact of the Madden-Julian oscillation on rainfall. *Geophys. Res. Lett.* **33**: L09704, DOI: 10.1029/2005GL025155

Ducet N, Le Traon PY, Reverdin G. 2000. Global high-resolution mapping of ocean circulation from TOPEX/Poseidon and ERS-1 and -2. *J. Geophys. Res.* **105**: 19477–19498.

Flatau M, Flatau P, Phoebus P, Niiler PP. 1997. The feedback between equatorial convection and local radiative and evaporative processes: the implications for intraseasonal oscillations. *J. Atmos. Sci.* **54**: 2373–2386.

Fu LL. 2007. Intraseasonal variability of the equatorial Indian Ocean observed from sea surface height, wind, and temperature data. *J. Phys. Oceanogr.* **37**: 188–202.

Fu LL, Christensen EJ, Yamarone CA, Lefebvre M, Menard Y, Dorrer M, Escudier P. 1994. TOPEX/Poseidon mission overview. *J. Geophys. Res.* **99**: 24369–24381.

Fu XH, Wang B. 2004. Differences of boreal summer intraseasonal oscillations simulated in an atmosphere–ocean coupled model and an atmosphere-only model. *J. Climate* **17**: 1263–1271.

Giese BJ, Harrison DE. 1990. Aspects of the Kelvin wave response to episodic wind forcing. *J. Geophys. Res.* **95**: 7289–7312.

Han W. 2005. Origins and dynamics of the 90-day and 30–60-day variations in the equatorial Indian Ocean. *J. Phys. Oceanogr.* **35**: 708–728.

Han W, Lawrence DM, Webster PJ. 2001. Dynamical response of equatorial Indian Ocean to intraseasonal winds: zonal flow. *Geophys. Res. Lett.* **28**: 4215–4218.

Harrison D, Vecchi G. 2001. January 1999 Indian Ocean cooling event. *Geophys. Res. Lett.* **28**: 3717–3720.

Heimbach P, Hill C, Giering R. 2005. An efficient exact adjoint of the parallel MIT General Circulation Model, generated via automatic differentiation. *Future Gener. Comput. Sys.* **21**: 1356–1371.

Hendon HH. 2000. Impact of air–sea coupling on the Madden–Julian oscillation in a general circulation model. *J. Atmos. Sci.* **57**: 3939–3952.

Hendon HH, Liebman B, Glick JD. 1998. Oceanic Kelvin waves and the Madden–Julian oscillation. *J. Atmos. Sci.* **55**: 88–101.

Inness PM, Slingo JM. 2003. Simulation of the Madden–Julian oscillation in a coupled general circulation model. Part I: Comparison with observations and an atmosphere-only GCM. *J. Climate* **16**: 345–364.

Izumo T, Masson S, Vialard J, Montegut CdB, Behera SK, Madec G, Takahashi K, Yamagata T. 2010. Low- and high-frequency Madden–Julian oscillations in austral summer: interannual variations. *Clim. Dyn.* **35**: 669–683.

Jones C, Waliser DE, Schemm JKE, Lau WKM. 2000. Prediction skill of the Madden and Julian Oscillation in dynamical extended range forecasts. *Clim. Dyn.* **16**: 273–289.

Kessler WS, McPhaden MJ. 1995. Oceanic equatorial waves and the 1991–93 El Niño. *J. Climate* **8**: 1757–1774.

Kessler WS, McPhaden MJ, Weickmann KM. 1995. Forcing of intraseasonal Kelvin waves in the equatorial Pacific. *J. Geophys. Res.* **100**: 10613–10631.

Klingaman NP, Weller H, Slingo JM, Inness PM. 2008. The intraseasonal variability of the Indian summer monsoon using TMI sea surface temperatures and ECMWF reanalysis. *J. Climate* **21**: 2519–2539.

Lau WKM, Waliser DE. (eds) 2005. *Intraseasonal variability in the atmosphere–ocean climate system*. Springer-Praxis: Heidelberg, Germany.

Le Traon PY, Dibarboure G, Ducet N. 2001. Use of a high-resolution model to analyze the mapping capabilities of multiple-altimeter missions. *J. Atmos. Oceanic Technol.* **18**: 1277–1288.

Liebmann B, Smith CA. 1996. Description of a complete (interpolated) outgoing longwave radiation dataset. *Bull. Am. Meteorol. Soc.* **77**: 1275–1277.

Madden RA, Julian PR. 1971. Detection of a 40–50 day oscillation in zonal wind in the tropical Pacific. *J. Atmos. Sci.* **28**: 702–708.

Madden RA, Julian PR. 1972. Description of global-scale circulation cells in the tropics with a 40–50 day period. *J. Atmos. Sci.* **29**: 1109–1123.

Marshall J, Hill C, Perelman L, Adcroft A. 1997a. Hydrostatic, quasi-hydrostatic, and non-hydrostatic ocean modeling. *J. Geophys. Res.* **102**: 5733–5752.

Marshall J, Adcroft A, Hill C, Perelman L, Heisey C. 1997b. A finite-volume, incompressible Navier–Stokes model for studies of the ocean on parallel computers. *J. Geophys. Res.* **102**: 5753–5766.

Matthews AJ. 2000. Propagation mechanisms for the Madden–Julian oscillation. *Q. J. R. Meteorol. Soc.* **126**: 2637–2651.

Matthews AJ. 2004. Atmospheric response to observed intraseasonal tropical sea surface temperature anomalies. *Geophys. Res. Lett.* **31**: L14107, DOI: 10.1029/2004GL020474

Matthews AJ. 2008. Primary and successive events in the Madden–Julian oscillation. *Q. J. R. Meteorol. Soc.* **134**: 439–453.

Matthews AJ, Hoskins BJ, Masutani M. 2004. The global response to tropical heating in the Madden–Julian oscillation during the northern winter. *Q. J. R. Meteorol. Soc.* **130**: 1991–2011.

Matthews AJ, Singhruck P, Heywood KJ. 2007. Deep ocean impact of a Madden–Julian oscillation observed by Argo floats. *Science* **318**: 1765–1768.

Matthews AJ, Singhruck P, Heywood KJ. 2010. Ocean temperature and salinity components of the Madden–Julian oscillation observed by Argo floats. *Clim. Dyn.* **35**: 1149–1168.

McCreary JP. 1983. A model of tropical ocean–atmosphere interaction. *Mon. Weather Rev.* **111**: 370–387.

McPhaden MJ. 1999. Genesis and evolution of the 1997–98 El Niño. *Science* **283**: 950–954.

Oliver ECJ, Thompson KR. 2010. Madden–Julian oscillation and sea level: Local and remote forcing. *J. Geophys. Res.* **115**: C01003, DOI: 10.1029/2009JC005337.

Rashid HA, Hendon HH, Wheeler MC, Alves O. 2011. Prediction of the Madden–Julian oscillation with the POAMA dynamical prediction system. *Clim. Dyn.* **36**: 649–661.

Reynolds RW, Smith TM, Liu C, Chelton DB, Casey KS, Schlax MG. 2007. Daily high-resolution-blended analyses for sea surface temperature. *J. Climate* **20**: 5473–5496.

Salby ML, Hendon HH. 1994. Intraseasonal behavior of clouds, temperature, and motion in the tropics. *J. Atmos. Sci.* **51**: 2207–2224.

Shinoda T, Hendon HH, Glick J. 1998. Intraseasonal variability of surface fluxes and sea surface temperature in the tropical western Pacific and Indian Oceans. *J. Climate* **11**: 1685–1702.

Webber BGM, Matthews AJ, Heywood KJ. 2010. A dynamical ocean feedback mechanism for the Madden–Julian oscillation. *Q. J. R. Meteorol. Soc.* **136**: 740–754.

Wheeler MC, Hendon HH. 2004. An all-season real-time multivariate MJO index: Development of an index for monitoring and prediction. *Mon. Weather Rev.* **132**: 1917–1932.

Woolnough SJ, Slingo JM, Hoskins BJ. 2000. The relationship between convection and sea surface temperature on intraseasonal timescales. *J. Climate* **13**: 2086–2104.

Woolnough SJ, Slingo JM, Hoskins BJ. 2001. The organization of tropical convection by intraseasonal sea surface temperature anomalies. *Q. J. R. Meteorol. Soc.* **127**: 887–907.

Wunsch C, Heimbach P. 2007. Practical global oceanic state estimation. *Physica D* **230**: 197–208.

Xie SP, Annamalai H, Schott FA, McCreary JP. 2002. Structure and mechanisms of South Indian Ocean climate variability. *J. Climate* **15**: 864–878.

Zhang CD. 2005. Madden–Julian oscillation. *Rev. Geophys.* **43**: RG2003, DOI: 10.1029/2004RG000158

